HAL open science

Simulation of ductile tearing during a full size test using a non local Gurson-Tvergaard-Needleman (GTN) model

Youbin Chen, Eric Lorentz, Anna Dahl, Jacques Besson

To cite this version:

Youbin Chen, Eric Lorentz, Anna Dahl, Jacques Besson. Simulation of ductile tearing during a full size test using a non local Gurson-Tvergaard-Needleman (GTN) model. Engineering Fracture Mechanics, 2022, 261, pp.108226. 10.1016/j.engfracmech.2021.108226 . hal-03799362

HAL Id: hal-03799362

https://hal.science/hal-03799362v1

Submitted on 5 Oct 2022

HAL is a multi-disciplinary open access archive for the deposit and dissemination of scientific research documents, whether they are published or not. The documents may come from teaching and research institutions in France or abroad, or from public or private research centers.

L'archive ouverte pluridisciplinaire **HAL**, est destinée au dépôt et à la diffusion de documents scientifiques de niveau recherche, publiés ou non, émanant des établissements d'enseignement et de recherche français ou étrangers, des laboratoires publics ou privés.

Simulation of ductile tearing during a full size test using a non local Gurson–Tvergaard–Needleman (GTN) model

Youbin Chen[a,b], Eric Lorentz[a], Anna Dahl[c], Jacques Besson[b]

[a] *IMSIA (UMR EDF-ENSTA-CNRS-CEA 9219), 7 Boulevard Gaspard Monge, Palaiseau 91120, France*
[b] *Mines ParisTech, PSL Research University, Centre des Matériaux, UMR CNRS 7633, 10 rue Henri Desbruères, Evry 91000, France*
[c] *EDF R&D, MMC, Lab Renardières, Avenue des renardières, Écuelles 77250, France*

Abstract

Ductile tearing of a full size precracked pipe is experimentally investigated. In order to model and interpret the test, the pipe material is characterized using smooth and notched tensile bars and precracked C(T) specimens. This experimental database is used to fit the parameters of the non local Gurson–Tvergaard–Needleman (GTN) proposed in [**?** **?**]. The model is used in finite element simulations using specific elements allowing for the control of strain/damage localization as well as volumetric locking. Mesh size independence is checked on notched tensile bars. The model is then able to represent the early stages of crack propagation in the pipe. In particular, experimentally observed crack branching is reproduced, whereas this appeared much more difficult to obtain using a local GTN model.

Keywords: Non local GTN model, Ductile failure, Large scale test

Nomenclature

a_0, a, Δa	initial, current crack length, crack advance
A_{nl}	non local thermodynamic force
B, B_n	thickness and net thickness of C(T) specimens
CMOD	Crack Mouth Opening Displacement
CTOD	Crack Tip Opening Displacement
$\boldsymbol{C}$	Cauchy–Green tensor
D_0, ΔD	initial minimum diameter, diameter variation
D_i, D_e	internal, external diameter
$\boldsymbol{E}$, $\boldsymbol{E}^e$, $\boldsymbol{E}^p$	strain tensor, elastic strain tensor, plastic strain tensor
$\tilde{\boldsymbol{E}}$	relaxed strain tensor
$\mathbb{E}$	fourth order elasticity tensor
E	Young's modulus
e_R	elongation at fracture
f_0, f, f_n	initial, total, nucleation porosity
f_c, f_F	porosity at coalescence, porosity at fracture
$\boldsymbol{F}$	deformation gradient tensor
F	force
g	hardening parameter (Voce law)
h	element size
J	volume variation ($J = \det \boldsymbol{F}$)
l	Lagrange multiplier
l_{nl}	internal length
λ	plastic multiplier
$\mathcal{N}$	nucleation rate
P	pressure
q_1, q_2	GTN model parameters
r	hardening parameter (Voce law)
r_{nl}, r_{inco}	penalization factors
R	notch radius
$R_{p0.2}$, R_m	0.2% proof stress, ultimate stress
S_0	initial minimum cross section
$\boldsymbol{T}$	stress tensor (work–conjugate of $\boldsymbol{E}$)
$\tilde{\boldsymbol{T}}$	stress tensor (associated to $\tilde{\boldsymbol{E}}$)
T_H, T_{eq}, $T_\star$	hydrostatic, von Mises, effective stress of $\boldsymbol{T}$
W	specimen width

ΔU	axial displacement
η, $\eta^\star$	stress triaxiality, modified stress triaxiality
Φ	global Helmholtz free energy
ϕ^e, ϕ^p	elastic and plastic parts of the local Helmholtz free energy
κ	isotropic hardening variable
$\overline{\kappa}$	non local hardening variable
Ω_0	domain in the initial configuration
$\boldsymbol{\sigma}$	Cauchy stress tensor
σ_0, σ_F	yield stress, flow stress
θ	volume variation

1. Introduction

The ATLAS+ European project is a 4–year European project launched in June 2017. Its main objective is to develop advanced structural assessment tools to address the remaining technology gaps for the safe and long term operation of nuclear reactor pressure coolant boundary systems. The transferability of ductile material properties from small scale fracture mechanics specimens to large scale components is one of the topics of the project. Within the project, a large experimental work was conducted to support the development and validation of advanced tools for structural integrity assessment. The experimental work is based on a comprehensive set of Fracture Mechanics experiments conducted on test specimens and large scale components together with a full characterization of the investigated materials (microstructure, plastic behavior). Within the framework of the project, three different materials were considered: a ferritic steel 15NiCuMoNb5 (WB36), an aged austenitic stainless steel weld and a VVER dissimilar metal weld.

This work focuses on the ferritic 15NiCuMoNb5 steel (WB36) and the use of assessment methods based on the Local Approach to Fracture methodology [**?**] applied to ductile rupture. Within this framework damage models describing nucleation, growth and coalescence of voids are used to represent material degradation up to full failure (see reviews in [**?** **?** **?**]). Due to their strong softening behavior and the resulting ill-posedness of the boundary value problem, the use of such models in standard displacement based finite element procedures leads to a well-known spurious mesh dependence. This includes the size, the type as well as the orientation of the elements [**?** **?**]. A pragmatic solution to bypass this problem is to only use elements having the same type (*e.g.* only bi-linear quadrangles with full integration), size and orientation in areas where cracks are growing [**?** **?**]. Finite element discretization is then used to represent the

geometry but also to control the fracture energy ; as such the element formulation becomes a model parameter. More recent and more satisfactory solutions consist in using non local models. They all allow introducing a material length used to control the fracture energy. Provided a sufficiently fine mesh is used to discretize the problem, convergence is attained and the solution becomes mesh independent. Most of non local formulations use extra degrees of freedom in addition to the displacements. Different formulations have been proposed over the years. Implicit gradient methods [? ?] facilitate the use of integral methods as originally proposed in [? ?]. Initially developed for quasi–brittle failure, these methods have also been used to model ductile fracture for metals within a finite strain framework [? ? ? ? ? ?]. Micromorphic models [?] use local state variables and their "micromorphic" counterparts. The free energy of the system depends on the gradient of the micromorphic variables and on coupling terms. This class of models can also be used to model ductile failure [? ?]. In particular, models based on a microdilatational theory [?] appear to be well suited to represent ductile damage by void growth. The last approach, so called non local gradient enhanced energy (GEE) model, only uses the gradient of a local state variable A decomposition–coordination technique is used to treat the non–locality. The variable of interest is duplicated: a first instance is used at the (global) scale of the structure, while a second instance is used at the (local) constitutive law level. As both variables reflect the same field, they should be equal. A Lagrange multiplier is introduced to weakly ensure this equality. The GEE model was first developed for quasi-brittle fracture [?] and was successfully extended to ductile rupture [? ?]. It was shown in [?] that this formulation is equivalent to a micromorphic model in which the coupling coefficient between local and non -local variables is very large (it then becomes a penalty factor used to enforce the equality between both variables). In that case, the GEE model exhibits much better convergence properties of the nonlinear solver than the micromorphic model. In this work, the GEE approach will be used together with the GTN model [?].

Ductile fracture is always accompanied by large plastic deformations. Although void growth and volume variation are usually accounted for, the material remains quasi-incompressible as the initial damage is in most cases very low. This may lead to a poor evaluation of pressure within the elements [?]. A common solution to this problem is to use bi–linear elements with selective integration [?]. This allows propagating cracks over large distances [? ?]. In the case of the above mentioned non -local formulations, elements use quadratic interpolations for the displacements and linear interpolations for the additional degrees of freedom needed to deal with non locality. In addition the use of

reduced integration is often not fully satisfactory. This problem can be solved using a Hu–Washizu type mixed finite element formulation as in [? ?]. This treatment of quasi–incompressibility was combined with the GEE formulation to address both numerical problems simultaneously [? ?]. This approach is used in the paper.

The use of damage models for ductile rupture to model crack initiation and propagation is nowadays routinely done for small size specimens using various damage models or intermediate size specimens (see *e.g.* [? ?]). In most cases, local models are used although applications to actual case studies using non local model can be found [? ? ? ? ?]. Applications to full size structures are less common. They are mostly based on the use of the Rice and Tracey model [?] as in [?] or of the local GTN model [? ? ? ? ? ?]. Applications of non local models for ductile rupture to large 3D structures have not yet been published to the knowledge of the authors. The goal of the present work is to apply the non local GTN model published in [? ?] to simulate a full size test conducted in the framework of the ATLAS+ project on the WB36 ferritic steel. The paper is organized as follows. The material and the experimental procedures are first presented. The main experimental findings are described in section 3. The non local GTN model used to carry out the simulations is recalled in 4. The model is tuned and applied to simulate axisymmetric notched bars and C(T) specimens in 5. Finally, the model is applied to simulate the full size structure in 6.

2. Materials and experimental procedures

2.1. Material

Tests were performed on a 15NiCuMoNb5 (WB36) ferritic steel representative of German PWR secondary feedwater lines. The material was supplied by Framatome GmbH in form of a forged pipe with a 378 mm external diameter and a thickness equal to 30 mm. The total length is 2200 mm. The chemical analysis of the material was carried out during the study. Results are shown in tab. 1. The microstructure of the material is shown in fig. 1 exhibiting a mixed ferriric/bainitic structure. For the full size test, the mock-up is obtained after welding a central section in ferritic steel (material WB36) with extension pipe (E355). The chemical analysis of the material supplied by the manufacturer is presented in tab. 2.

C	Si	Mn	P	S	Cr	Mo	Ni	
0.14	0.31	0.94	0.009	0.02	0.4	0.35	1.14	
Al	Sn	Cu	As	N	V	Nb	O	Fe
0.15	0.13	0.62	—	0.013	—	0.03	0.003	bal.

Table 1: Chemical composition (wt. %) of the 15NiCuMoNb5 ferritic steel (WB36).

C	Si	Mn	P	S	Cr	Mo	Ni	
0.17	0.4	1.56	0.016	0.006	0.17	0.02	0.01	
Al	Sn	Cu	As	N	V	Nb	O	Fe
0.028	—	00.03	—	0.008	0.09	0.004	n.a.	bal

Table 2: Chemical composition (wt. %) of the extension pipe (E355).

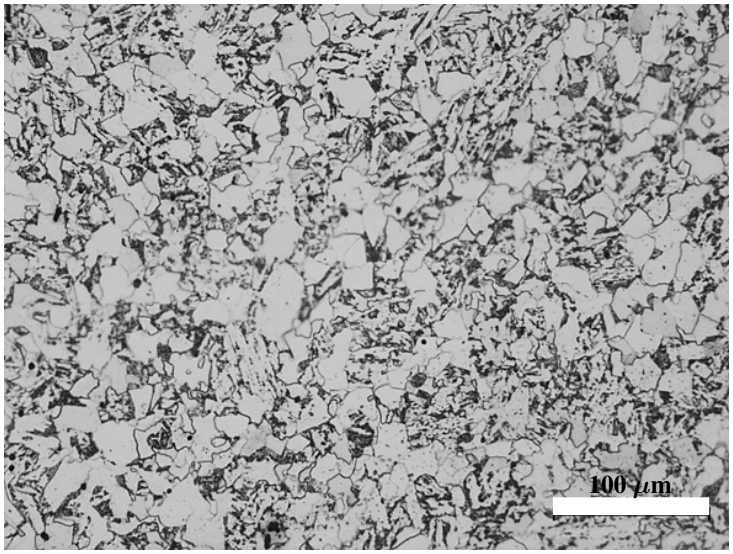

Figure 1: Microstructure of the WB36 material.

2.2. Material characterization procedures

The material was tested at room temperature using smooth tensile bars (ST6 — The diameter is equal to 6 mm), axisymmetric notched tensile (NT) bars and Compact Tension (C(T)20) specimens. All specimens were extracted from the forged pipe. In the following, axisymmetric notched bars are referred to as NT_χ where $\chi = 10R/D_0$ with R the initial notch radius and D_0 the initial minimum diameter. Three different notch radii are used with $\chi = 2,\ 4,\ 10$. The geometry of the tensile bar and the NT_χ bars are shown in fig. 2. The geometry of C(T)20 follows the ASTM–1820 standard. The total thickness is $B = 20$ mm and the net thickness after machining with side grooves is $B_n = 16$ mm. An initial sharp notch was first machined with side grooves corresponding to 10% of the total thickness. Fatigue precracking was then conducted in order to obtain an initial crack having a length $a_0 \approx 24$ mm corresponding to a crack length to width ratio $a/W = 0.6$. The C(T) specimens were finally machined to obtain side grooves corresponding to 20% of the total thickness. Using this preparation procedure allows obtaining straight initial crack fronts. All test specimens were loaded, so that the loading direction is the pipe longitudinal axis which is the main loading direction of the pipe during bending.

Elongation in smooth tensile specimens was measured with an extensometer having a 27 mm gage length. The axial displacement in NT_χ specimens was measured using an extensometer having a 25 mm gage length positioned symmetrically with respect to the notch . In addition, the variation of the minimum diameter for NT_χ specimens was tracked using a video system (acquisition frequency 1 Hz) already described in [**?**]. The diameter variation was also measured using a radial extensometer. Both sets of measurements are in good agreement, as shown below in fig. 6.

Compact Tension (C(T)20) specimens were tested according to the ASTM E1820 procedure to determine the J—Δa curves. The partial unloading technique was used to determine crack advance (Δa). After testing, specimens were heat treated to mark the crack size on the fracture surface and were then broken in liquid nitrogen.

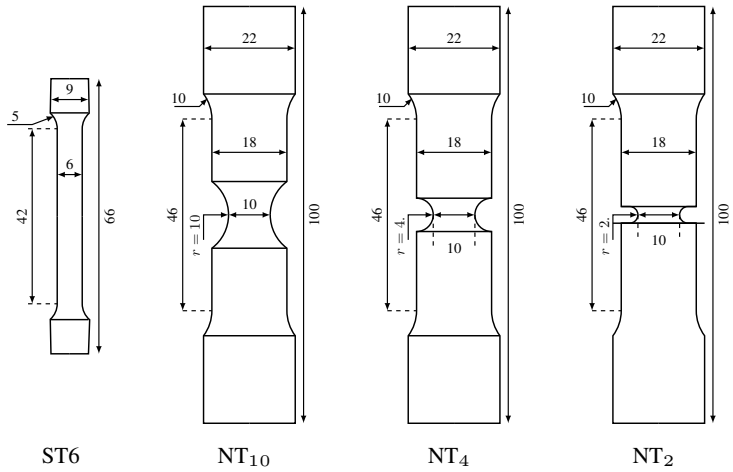

Figure 2: Geometries of the smooth tensile specimen ST6, Notch tensile specimens NT_2, NT_4 and NT_{10} (unit: mm).

2.3. Full size test

The full size test was performed by EDF R&D under 4–point bending at room temperature on a pipe containing a through wall crack. The geometry of the pipe, called FP1 mock-up, is shown in fig. 3–a. The central section of the pipe is made of the WB36 material, while the two extensions are made of the E355 steel. The initial through–wall crack introduced by EDM and fatigue pre–cracking is located on the x—y cross-section plane (or $z = 0$ plane in cylindrical coordinate system), as shown in fig. 3–b. Fig. 3–a shows the FP1 pipe before the bending test. The initial through–wall crack is clearly visible in this figure.

The setup for the 4–point bending test (Fig. 4), designed by EDF R&D, is fitted for a 5000 kN testing machine. The force applied on the pipe was measured using a load cell. Crack opening was measured using a clip gage. The pipe deflection was measured using a linear variable differential transformer (LVDT). One major objective of the test is the detection of ductile crack initiation and the measurement of ductile crack extension during the experiment.

(a) View of the FP1 pipe.

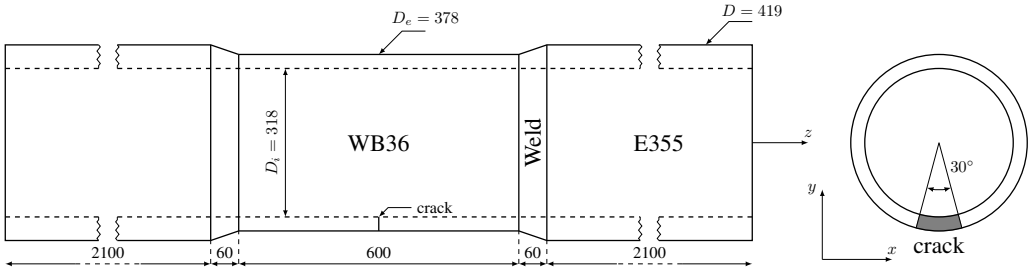

(b) Geometry of the FP1 pipe (unit: mm).

Figure 3: Full size test (FP1 pipe).

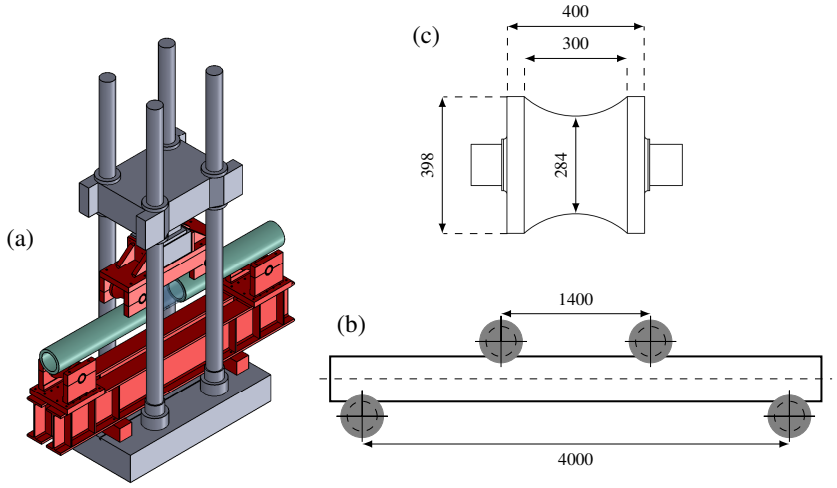

Figure 4: EDF R&D 4–point bending frame for testing mock-ups (length units in mm): (a) Overall view of the setup. (b) 4–point bending test showing the pipe and the four indentical rollers. (c) Detailed view of the diabolo–shaped rollers.

3. Experimental results

3.1. Tensile tests

Fig. 5 shows the true stress-strain curves obtained on the WB36 ferritic steel for a strain rate equal to $5.\,10^{-4}$ s^{-1}. In total, 13 smooth tensile specimens were tested for different angular positions. These results evidence the inhomogeneity with respect to the angular position of the tensile properties of the material. Such an inhomogeneity was already observed in similar thick walled components [**?**]. The relative standard deviation is around 3%. Besides, it is observed that the yield stress σ_0 is approximatively 500 MPa. For some specimens a short Lüders plateau is observed.

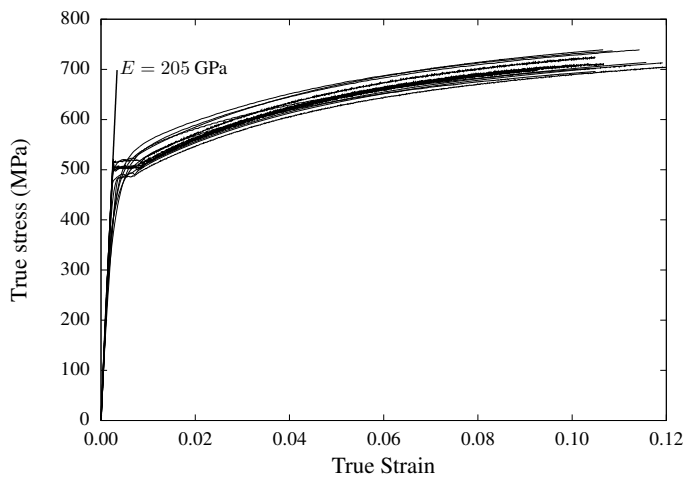

Figure 5: Stress—strain curves for the WB36 pipe material. 13 tests are shown.

Additional tests were also performed on the E355 material which is used for the extension arms. Specimens were extracted at various locations. Tensile properties are given in tab. 3.

Position	E (GPa)	$R_{p0.2}$ (MPa)	R_m (MPa)	e_R (%)	Z (%)
outer diameter	205	374	555	39	79
center		387	578	32	72
inner diameter		386	577	36	75

Table 3: Tensile properties of the bending arms material (E355) at room temperature. E: Young's modulus, $R_{p0.2}$: 0.2% proof strength, R_m: ultimate stress, e_R: elongation at fracture, Z: reduction of area.

3.2. Notched tensile specimens

Fig. 6–a shows the measured average stress at the minimum cross section, F/S_0 (F: force, S_0: initial minimum cross section), as a function of the axial displacement (ΔU). Fig. 6–b shows the average stress—relative diameter reduction ($\Delta D/D_0$) curves for NT$_\chi$ specimens (ΔD: diameter variation, D_0 initial minimum diameter). Maximum load increases with decreasing the notch radius as often observed in the literature [**? ?**]. The sudden load drop observed on the specimens corresponds to crack initiation. Ductility, defined as the diameter reduction at crack initiation, decreases with decreasing the notch radius . These well understood evolutions [**?**] are caused by the increase of stress triaxiality at the center of the specimens as the notch radius decreases. In fig. 6–b, diameter reductions measured by the extensometer (dashed lines) and the video system (solid lines) are in close agreement. The sharp load drop can only be recorded using the extensometer as the acquisition rate of the video system is too slow (1 Hz) to capture failure. All notched bars were extracted from the same angular sector in the pipe. For that reason much less scatter is observed compared to tests carried out on tensile bars.

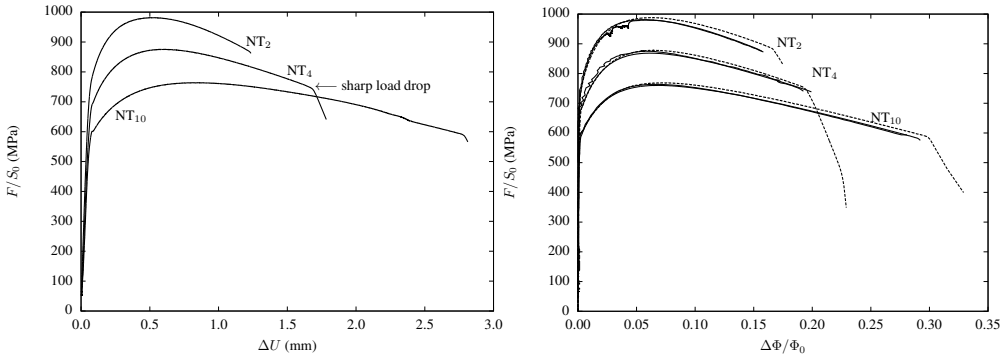

Figure 6: NT$_\chi$ tests. (a) Average stress — axial displacement curves. (b) Average stress — relative diameter reduction curves. Solid lines: video system. Dashed lines: extensometer.

3.3. Compact tension specimens

Fig. 7–a shows the Force—CMOD curves for the nine tests performed on C(T)20 specimens. Differences are observed among the results which are mainly due to slightly different initial crack lengths (a_0) and possibly to the inhomogeneity of the material. Fig. 7–b shows the fracture surface of one C(T) specimen. All fracture surfaces on C(T) specimens share the same characteristics. In addition, in most cases, the fracture surface is rather flat.

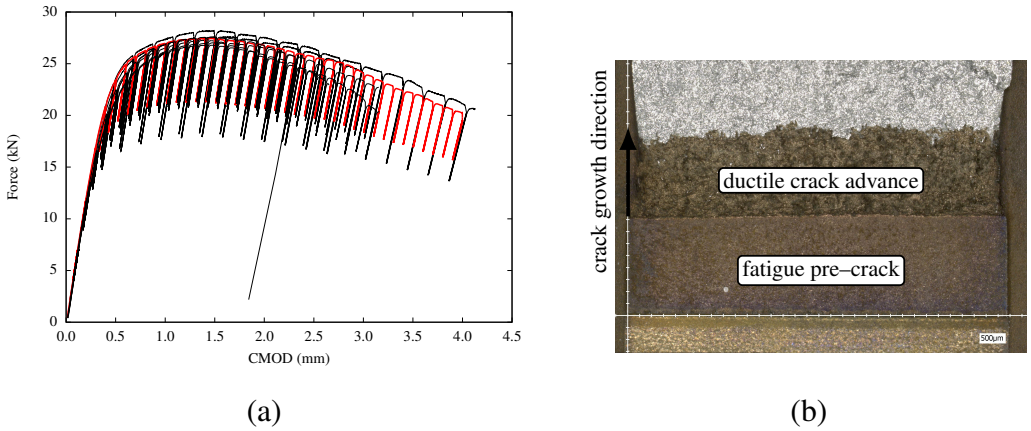

(a) (b)

Figure 7: C(T)20 tests. (a) Force—CMOD curves. The red curve corresponds to the specimen shown in (b). (b) Macroscopic view of ductile crack extension (dark area).

3.4. Large-scale test

Fig. 8–a shows the pipe during the test and fig. 8–b shows the corresponding experimental Force—CMOD curve. Several unloads were performed to monitor stiffness changes due to crack advance and plastic deformation. Two large unloads (95% of the measured load) were also performed so as to create beach marks on the crack path. The pipe was fully unloaded for a CMOD of about 18 mm. During the test, two methods to detect the initiation of ductile tearing were used. First, partial unloadings were performed to measure the variation of the pipe compliance due to crack advance. The analysis of these measurements (not detailed here) indicates that crack initiation occurred between the unloadings performed for CMOD$=1.2$ mm and CMOD$=3.1$ mm. Second, a potential–drop monitoring system was used. The potential between both sides of the machined defect was measured at seven locations on the outer skin of the pipe (see fig. 10). A clear variation of the potential was detected for all measurement points for a CMOD larger than 2.3 mm which is therefore considered as the CMOD at crack initiation.

Fig. 9 shows the outer surface of the pipe after the test was stopped. It can be observed that at both ends ($\pm 15°$) of the initial crack, two cracks have initiated and propagated. The main cracks propagated during the entire test, whereas the secondary cracks stopped after a limited advance.

After the test, the crack was further grown by fatigue so as to facilitate the cutting of the fracture surface. A 3D scan of the cracked area is shown in fig. 10–a.

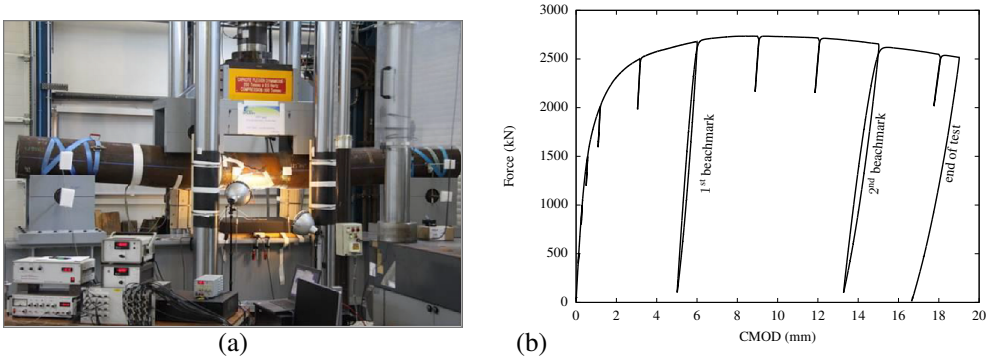

Figure 8: (a) View of the pipe during the test. Pipe deflection is clearly visible. (b) Force—CMOD curves.

Crack propagation starts at the center of the wall thickness (red arrows). A flat triangular area is then formed (see also fig. 11) as often observed in sheet metals [**?** **?**]. The cracks then tilt. The crack path is summarized by the diagram in fig. 10–b. Crack bifurcation is observed and appears to have started at the early stage of crack propagation. This corresponds to a macroscopic deflection (tilt) from the initial crack plane. In addition the path is slanted (twist) with respect to the main crack propagation direction. This crack propagation mode is often observed in metal sheets [**?** **?**]. The thin green dashed lines represent the crack path that would have been observed in absence of tilt.

Closer views of the crack paths at both ends ($\pm 15°$) of the initial crack are shown in fig. 11. On these images, the initial flat advance is represented by the blue shaded area. Its maximum advance, at the center of the pipe wall, is about 10 mm. Red lines are plotted to indicate the first and second beach marks (also shown by yellow arrows on the pipe) which correspond to the full unloadings performed during the test. Crack advance at both ends of the initial crack appears to be slightly non–symmetric. On both sides of the flat zone, shear lips can also be observed. They ultimately joint to form the slanted crack path. In particular, the first beach mark (CMOD$\approx$6 mm) is located in this zone. The intersection between the red line (beach mark) and the blue line (flat crack area) indicates that the maximum crack propagation is between 4 and 6 mm in the initial crack plane for a CMOD of about 6 mm. This is a typical value that can be used to validate the simulation results. At the outer diameter, the secondary cracks can also be observed.

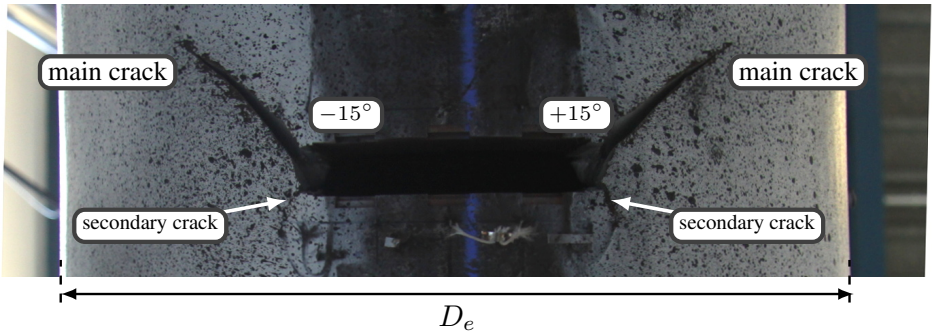

Figure 9: Outer view of the cracked pipe after the test was stopped showing both mains cracks and secondary cracks.

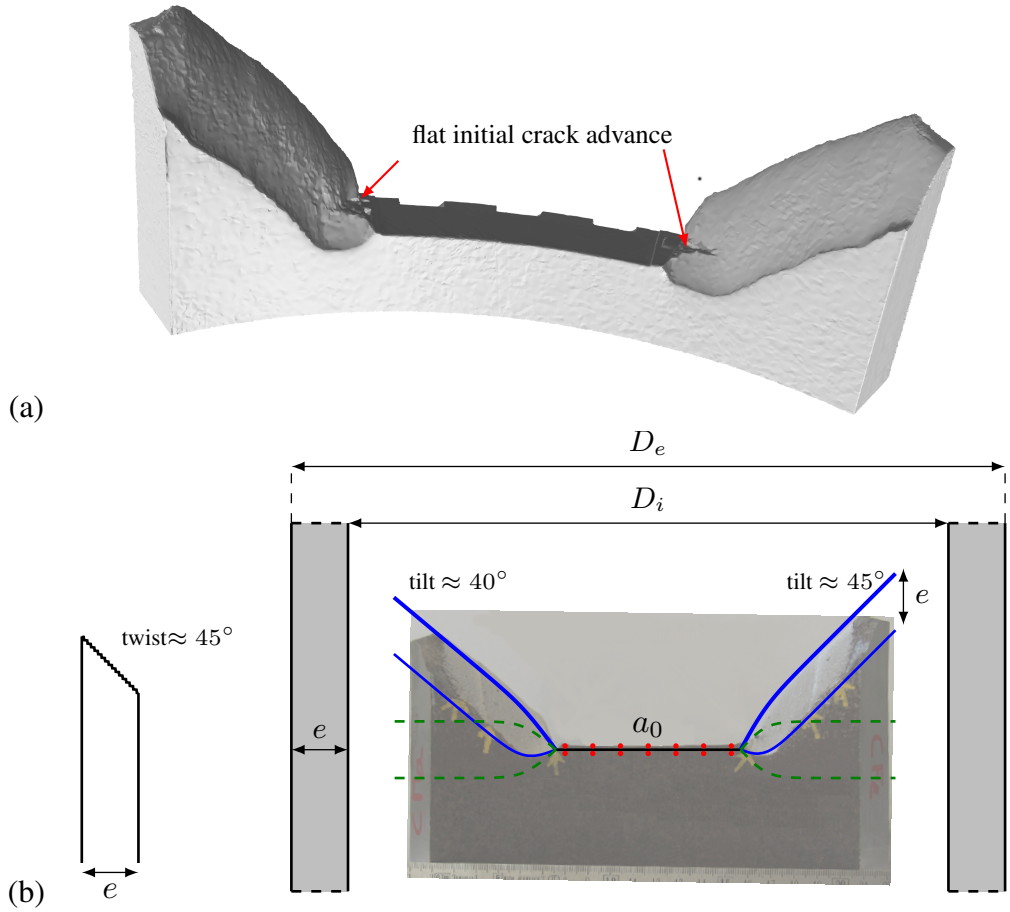

Figure 10: (a) 3D scan of the initial defect and crack propagation. (b) Schematic view of the crack path. The blue lines indicate the crack path on the external (thick lines) and internal (thin lines) diameters of the pipe. The thin green dashed lines represent the crack path in absence of tilt. Red dots indicate the position of the seven potential drop measurements.

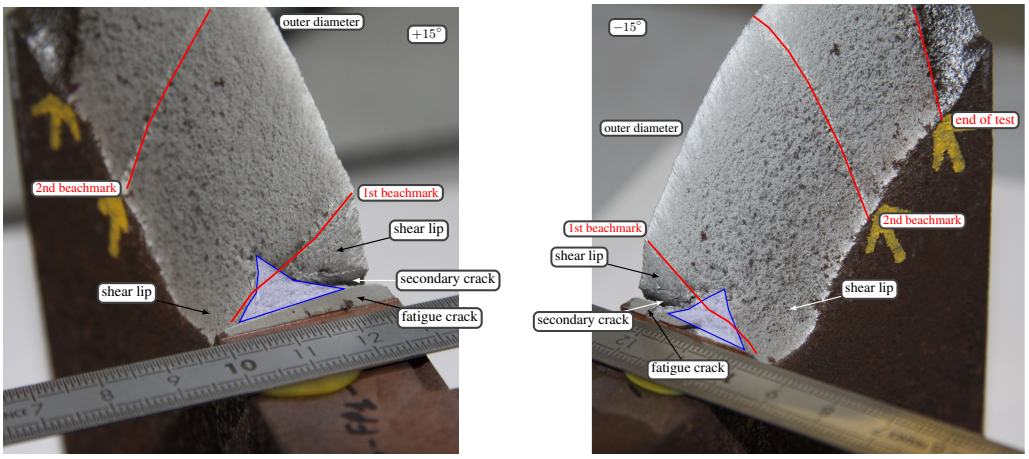

(a) at $+15°$ (b) at $-15°$

Figure 11: View of crack bifurcation at both ends of the initial crack after the paper was ...

4. A non local GTN model

In this section, a non local GTN model is summarized. It was originally proposed in [**?**] to handle the issues of spurious localization. Its applications to small–scale yielding loading was studied in [**?**].

4.1. Finite strain modeling

Ductile failure is always accompanied by large plastic strains. Therefore a finite strain framework must be used. In this work, the finite strain formulation proposed in [**? ?**] is used. The strain tensor $\boldsymbol{E}$ is defined as:

$$\boldsymbol{E} = \frac{1}{2}\log\left(\boldsymbol{F}^T.\boldsymbol{F}\right) = \frac{1}{2}\log\left(\boldsymbol{C}\right) \tag{1}$$

where $\boldsymbol{F}$ is the deformation gradient tensor and $\boldsymbol{C} = \boldsymbol{F}^T.\boldsymbol{F}$ is the Cauchy–Green strain tensor. It is assumed that the logarithmic strain tensor can be split into an elastic ($\boldsymbol{E}^e$) and a plastic part ($\boldsymbol{E}^p$) as follows:

$$\boldsymbol{E} = \boldsymbol{E}^e + \boldsymbol{E}^p \tag{2}$$

The stress tensor $\boldsymbol{T}$ is defined as the work-conjugate of $\boldsymbol{E}$. Finally, only pure isotropic hardening is considered. It is characterized by a unique scalar variable referred to as κ. The material state is therefore described by the strain tensor $\boldsymbol{E}$, the hardening variable κ and the plastic strain tensor $\boldsymbol{E}^p$.

4.2. Non local Gradient Enhanced Energy model and its relaxed formulation

In order to handle the issue of strain localization, a non local Gradient Enhanced Energy (GEE) model is used. It is based on the introduction of the gradient of the hardening variable κ into the global Helmholtz free energy Φ since κ may reflect localization due to both plasticity and plasticity–induced damage:

$$\begin{aligned}\Phi(\boldsymbol{E}, \boldsymbol{E}^p, \kappa) &= \int_{\Omega_0} \left(\phi^e(\boldsymbol{E}^e) + \phi^p(\kappa)\right)\, d\Omega_0 + \int_{\Omega_0} \frac{1}{2}\sigma_0 l_{\text{nl}}^2 \nabla\kappa.\nabla\kappa\, d\Omega_0 \\ &\equiv \Phi_1(\boldsymbol{E}, \boldsymbol{E}^p, \kappa) + \int_{\Omega_0} \frac{1}{2}\sigma_0 l_{\text{nl}}^2 \nabla\kappa.\nabla\kappa\, d\Omega_0\end{aligned} \tag{3}$$

where ϕ^e and ϕ^p are the elastic and plastic parts of the local Helmholtz free energy density. ϕ^e is simply expressed as $\phi^e = \frac{1}{2}\boldsymbol{E}^e : \mathbb{E} : \boldsymbol{E}^e$ where $\mathbb{E}$ is the fourth order elasticity tensor (assumed isotropic in the following). Ω_0 is the body domain in the initial configuration, σ_0 is the yield stress and l_{nl} an internal length. l_{nl} is therefore

a parameter which weights the non local interactions among neighboring material points. It has been shown in [**?**] that the width of localization bands is about equal to $(1.3 \pm 0.2) l_{\text{nl}}$. It was shown in [**?**] that the thermodynamic driving force [**?**] associated to κ is:

$$A_{\text{nl}} = -\frac{\partial \phi^p}{\partial \kappa} + \text{div}\left(\sigma_0 l_{\text{nl}}^2 \nabla \kappa\right) \tag{4}$$

In this equation $\partial \phi^p / \partial \kappa$ corresponds to the work hardening *i.e.* $\sigma_F(\kappa) - \sigma_0$ where σ_F is the flow stress of the damage free material. Obviously, an additional nonlinearity appears due to the divergence term in A_{nl}. In order to reduce this nonlinearity, following Lorentz *et al.* [**?**], a decomposition-coordination technique as proposed by Fortin and Glowinski [**?**] is used. The hardening variable κ is duplicated: a first instance (named $\overline{\kappa}$) is used at the (global) scale of the structure while a second instance (still named κ) is used at the (local) constitutive equations level. A Lagrange multiplier l is introduced to weakly enforce the equality between $\overline{\kappa}$ and κ. The corresponding augmented Lagrangian is then expressed as:

$$\begin{aligned} L_{\text{nl}}(\boldsymbol{E}, \boldsymbol{E}^p, \kappa, \overline{\kappa}, l) &= F_1(\boldsymbol{E}, \boldsymbol{E}^p, \kappa) + \\ & \int_{\Omega_0} \left(\frac{1}{2} \sigma_0 l_{\text{nl}}^2 \nabla \overline{\kappa}.\nabla \overline{\kappa} + l(\overline{\kappa} - \kappa) + \frac{1}{2} r_{\text{nl}} (\overline{\kappa} - \kappa)^2 \right) d\Omega_0 \end{aligned} \tag{5}$$

The augmentation term $\frac{1}{2} r_{\text{nl}} (\overline{\kappa} - \kappa)^2$ was introduced in [**?**] to avoid possible oscillations of the plastic strain, as numerically shown in [**?**].

In quasi-incompressible situations, volumetric locking may appear. To solve this problem, the Hu-Washizu mixed variational principle [**?**] is used. Volume variation is denoted $J = \det \boldsymbol{F}$ and one can show that trace$(\boldsymbol{E}) = \log J$. An additional degree of freedom θ is introduced to describe volume variations at the global level. A Lagrange multiplier P ensures the weak equality between $\log J$ and θ. This leads to the following augmented Lagrangian which allows solving simultaneously strain/damage localization and volumetric locking:

$$\begin{aligned} L(\boldsymbol{E}, \boldsymbol{E}^p, \kappa, \overline{\kappa}, l, \theta, P) &= L_{\text{nl}}(\tilde{\boldsymbol{E}}, \boldsymbol{E}^p, \kappa, \overline{\kappa}, l) + \\ & \int_{\Omega_0} \left(P(\log J - \theta) + \frac{1}{2} r_{\text{inco}} (\log J - \theta)^2 \right) d\Omega_0 \end{aligned} \tag{6}$$

where $\tilde{\boldsymbol{E}}$ is the relaxed strain tensor used in the constitutive law:

$$\tilde{\boldsymbol{E}} = \boldsymbol{E} + \frac{1}{3} \left(\theta - \text{trace}(\boldsymbol{E})\right) \mathbf{1} \tag{7}$$

where $\mathbf{1}$ is the identity second order tensor. The augmentation term $\frac{1}{2}r_{\text{inco}}(\log J - \theta)^2$ was introduced in [**?**] to avoid oscillations of the plastic strain. It was shown in [**?**] that the (constitutive) stress tensor and the driving force associated to κ are now:

$$\tilde{\boldsymbol{T}} = \mathbb{E} : (\tilde{\boldsymbol{E}} - \boldsymbol{E}^p) \tag{8}$$

$$A_{\text{nl}} = -\frac{\partial \phi^p}{\partial \kappa} + l + r_{\text{nl}}(\overline{\kappa} - \kappa) \tag{9}$$

Compared to eq. 4, the divergence term in the driving force associated to κ is replaced by $l + r_{\text{nl}}(\overline{\kappa} - \kappa)$. Consequently, A_{nl} is chosen in the following to express the constitutive equations.

4.3. Finite element discretization

The expression of the Lagrangian of the system (eq. 6) leads to a finite element formulation which was detailed in [**?** **?**]. This formulation will not be described here. Suffice to say that the finite elements make use of five nodal variables $(\underline{\boldsymbol{u}}, \overline{\kappa}, l, P, \theta)$ where the vector $\underline{\boldsymbol{u}}$ represents the displacements. This formulation is referred to as "5–field formulation" in the following. Displacements are discretized using quadratic interpolations. All other variables $(\overline{\kappa}, l, P, \theta)$ are discretized using linear interpolations. In all cases, reduced Gauss integration is used. Examples of non local locking–free elements with reduced integration are shown in fig. 12. The average number of degrees of freedom per element is 10 for 2D quadrilateral elements and 16 for 3D hexahedra.

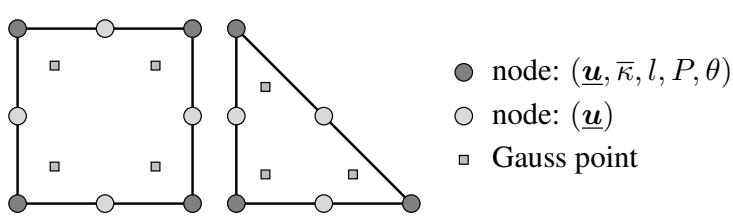

Figure 12: Examples of non local locking–free finite elements with reduced integration: quadrilateral element and triangular element

4.4. Corresponding GTN constitutive law

The formulation proposed above to handle quasi–isochoric plasticity and gradient hardening was presented without referring to any particular plasticity model. This generic framework is now applied to the GTN model [**?**]. It describes the behavior of ductile metals containing voids. Work hardening is still assumed to be isotropic and described by a single scalar variable κ. The porosity (void volume fraction) f is considered as the only isotropic damage variable. For the sake of simplicity, the strain tensor $\tilde{\boldsymbol{E}}$ and the stress tensor $\tilde{\boldsymbol{T}}$ used in the constitutive law will be denoted $\boldsymbol{E}$ and $\boldsymbol{T}$, respectively. Following [**?**], the GTN model is used to define the scalar stress measure $T_\star$:

$$G(T_H, T_{\text{eq}}, T_\star) = \frac{T_{\text{eq}}^2}{T_\star^2} + 2q_1 f_\star \cosh\left(\frac{3}{2} q_2 \frac{T_H}{T_\star}\right) - 1 - q_1^2 f_\star^2 \overset{\text{def. T}_\star}{=} 0 \tag{10}$$

where T_{eq} and T_H are the von Mises and hydrostatic stresses. Parameters q_1 and q_2 are two material constants and $f_\star$ is the effective porosity which is a function of the porosity f so as to account for the rapid drop in the stress carrying capacity when void coalescence starts:

$$f_\star = \begin{cases} f & \text{if } f < f_c \\ f_c + \dfrac{1/q_1 - f_c}{f_F - f_c}(f - f_c) & \text{otherwise} \end{cases} \tag{11}$$

where f_c and f_F represent the porosity at the onset of coalescence and the porosity at fracture. The evolution of f is given by the sum of the rate of void growth $\dot{f}_g$ and the rate of void nucleation $\dot{f}_n$:

$$\dot{f} = \dot{f}_g + \dot{f}_n = (1 - f)\text{trace}\dot{\boldsymbol{E}}^p + \mathcal{N}(\kappa)\dot{\kappa} \tag{12}$$

In the previous equation the first term of the right hand–side corresponds to void growth, whereas the second correspond to strain controlled void nucleation [**?**]. In the present study, damage is assumed to be controlled by void growth and void coalescence only, so $\mathcal{N}(\kappa) = 0$. Void nucleation could here be used to represent nucleation of secondary voids on iron carbides at high deformation levels which leads to the formation of small dimples on the fracture surfaces [**?**]. In this study it appeared to be sufficient to use the $f_\star$ function to model final failure. As long as there is no rotation of the eigenbasis of the stress tensor, the scalar stress measure $T_\star$ and $\sigma_\star$ are linked by $T_\star = J\sigma_\star$ [**?**]. Therefore, the yield function $\mathcal{F}$ can be expressed as:

$$\mathcal{F} = \frac{T_\star}{J} - (\sigma_F - A_{\text{nl}}) = 0 \tag{13}$$

where the expression of the driving force A_{nl} is given in eq. 9. The Kuhn–Tucker consistency conditions [**?**] are then:

$$\lambda \geq 0,\ \mathcal{F} \leq 0,\ \lambda\mathcal{F} = 0 \tag{14}$$

where λ denotes the plastic multiplier. The plastic strain rate tensor $\dot{\boldsymbol{E}}^p$ and the the rate of the hardening variable κ are then given by:

$$\dot{\boldsymbol{E}}^p = \lambda \frac{\partial \mathcal{F}}{\partial \boldsymbol{T}} = \frac{\lambda}{J} \frac{\partial T_\star}{\partial \boldsymbol{T}} \qquad \dot{\kappa} = \lambda \frac{\partial \mathcal{F}}{\partial A} = \lambda \tag{15}$$

The present model does not account for a possible dependence of the damage kinetics on the third stress invariant (or Lode angle). Models including this dependence (see *e.g.* [**? ? ? ?**]) have been proposed in the literature. However, the dependence on the third invariant appears not to be needed at high triaxiality as shown in [**?**]. In this paper, the original Nahshon&Hutchinson model [**?**] is modified, so that the dependence on the third invariant disappears at high triaxialities (above 0.5 to 0.7 in the paper). For this reason the effect of the third invariant was not included in the present model as high stress triaxialities are obtained for all specimens of the experimental database. Note that such as dependence can indeed be included in the non–local treatment of failure [**? ?**].

5. Finite element simulations

5.1. Simulation techniques

The non local GTN model was both implemented in Code_Aster (software for finite element analyses), developed at EDF, and Zset, developed at Centre des Matériaux and ONERA [**? ?**] [1]. Very close agreement was obtained when comparing results obtained using both codes. An implicit time–discretization with respect to κ and an explicit update with respect to the porosity f are used to integrate the constitutive equations. A material point is considered as broken when f reaches f_F. The notched tensile specimens are meshed using axisymmetric elements while the other specimens (the compact tension specimen C(T)20 and the FP1 large-scale structure FP1) are meshed using 3D elements. In all cases, 5–field finite elements with 2×2 (quadrilateral elements) or $2 \times 2 \times 2$ (hexahedron elements) integration points per element are used. The element size (h) is close to 0.1 mm in areas where cracks propagate. As explained below, this element size

[1] see `https://www.code-aster.org` and `http://www.zset-software.com`

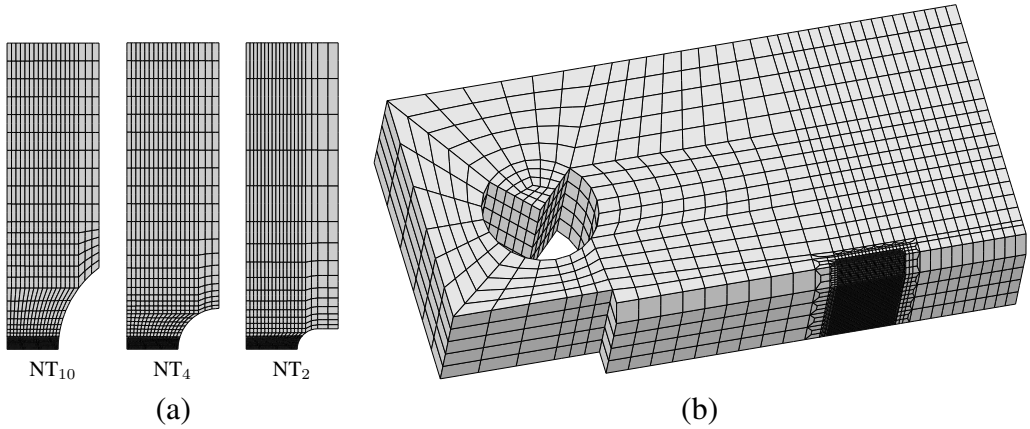

Figure 13: Meshes for (a) NT_2, NT_4, NT_{10} and (b) C(T)20 specimens.

assures to obtain converged results and to have a tractable number of degrees of freedom in the full-scale simulation. Meshes of NT and C(T)20 specimens are shown in fig. 13. Usual symmetry conditions are accounted for in order to reduce the size of the simulations hence also precluding non symmetric damage distribution. The resulting meshes for the NT and C(T) specimens have $\sim 10,000$ and $\sim 400,000$ degrees of freedom.

5.2. Identification procedure

Material parameters describing the elasto–plastic behavior of the WB36 material are identified using test results on notched bars before the sharp load drop which corresponds to failure initiation (see fig. 6). As the initial damage is very low and hardly affects the overall behavior, the identification is performed without accounting for damage or non local effects. The Young modulus is measured during tensile tests: $E = 205$ GPa. Poisson ratio is set to 0.3 (usual value for steel). The flow stress is then expressed as:

$$\sigma_F(\kappa) = \sigma_0 + r(1 - \exp(-g\kappa)) \tag{16}$$

This simple Voce law allows obtaining a good fit over the entire plastic strain range including post-necking behavior characterized using NT_χspecimens ($0 \leq \kappa \leq 0.6$). The resulting flow curve corresponds to the lowest values obtained during tensile tests (Fig. 5).

Five parameters are needed to describe damage by void growth and coalescence: the initial porosity f_0 and the GTN parameters q_1, q_2, f_c and f_R. Examinations of the fracture surfaces have shown that primary dimples were initiated on manganese sulfide inclusions. Oxides were rarely detected. Consequently the initial porosity can be evaluated using the Franklin formula [**?**] (the effect of oxygen is neglected) assuming that MnS inclusions debond from the matrix to form voids for very low plastic strain levels:

$$f_{\text{MnS}} \equiv f_0 = 0.054 \left(C_{\text{S}} - \frac{0.001}{C_{\text{Mn}}} \right) = 0.001 \tag{17}$$

where C_{S} and C_{Mn} respectively stand for the sulfur and manganese weight content (values are given in tab. 1). q_1 was set to 1.5. f_c set to 0.05 which is a value within the ranges obtained with unit cell simulations [**?** **?**]. f_F is set to 0.25. Using these values together with $q_2 = 1$ as in many other studies did not lead to a good fit for the tests on NT_χ specimens, so that q_2 was adjusted on the load—diameter reduction curves.

Finally, an internal length equal to 0.3 mm was chosen as it allows representing both NT and C(T) tests. Using this value, a mesh size $h \approx l_{\text{nl}}/3 = 0.1$ mm can be used to obtain reasonnably mesh size independent results [**?**]. Numerical parameters r_{nl} and r_{inco} were chosen following recommendations given in [**?**]. All material parameters are gathered in tab. 4.

Mesh size convergence is checked on fig. 14 for NT_2 specimens by varying the mesh size between 300 and 75μm. Before sharp load drop (crack initiation at the center of the minimum cross section), results appear to be mesh independent. This is because damage is not localized at this stage. It is noticeable that results for $h = 100\mu$m and $h = 75\mu$m are similar when the load is sharply decreasing (crack initiation and propagation from the center of the minimum cross section) showing that convergence is achieved for these element sizes. Convergence of the non local GTN model in cracked structures was previously checked in [**?**]. In addition, a simulation assuming no damage growth shows that simulation results are hardly affected by damage development before crack initiation as assumed to fit the hardening law, thus validating the strategy for its fit.

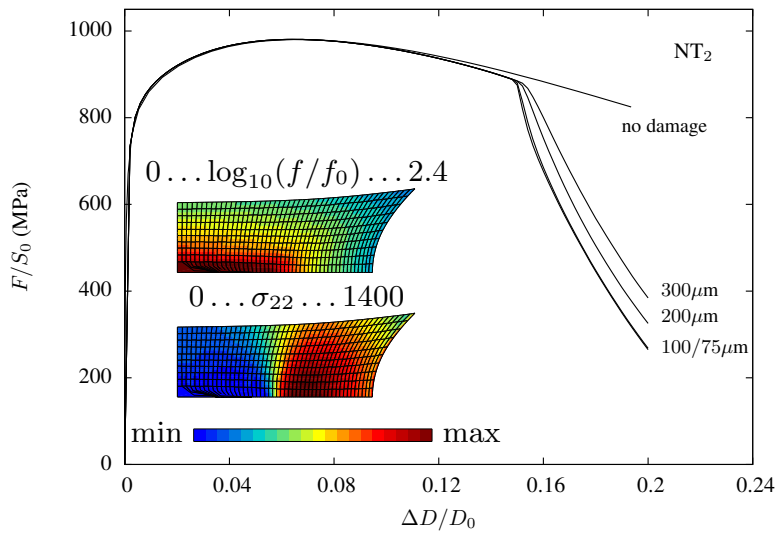

Figure 14: Simulation of the NT_2 specimen with various mesh sizes. Contour plots show values of the opening stress (MPa) and damage during crack propagation from the center of the specimen.

Elasticity	Young's modulus E	205 GPa
	Poisson ratio ν	0.3
Plasticity	σ_0 (MPa)	500
	r, g	318 MPa, 9.1
Damage	initial porosity f_0	0.001
	f_c, f_R	0.05, 0.25
	q_1, q_2	1.5, 1.14
Non local model	l_{nl}	0.3 mm
Penalty parameters	r_{nl}	5000 MPa
	r_{inco}	5000 MPa
Mesh size	h	0.1 mm

Table 4: Material parameters.

5.3. Model validation on NT specimens

As mentioned in the previous part, the experimental results on NT2 were used to fit the plasticity parameters and the damage parameters. These parameters were then used to predict plasticity and the fracture points for NT4 and NT10, as well as the global behavior of C(T)20 specimens. Fig. 15 compares the experimental and simulated force—displacement and force—diameter reduction curves for NT_2, NT_4 and NT_{10} specimens. As can be seen in this figure, a very good fit for the plastic behavior is obtained. Fracture initiation points are also well predicted but the model tends to slightly overestimate ductility.

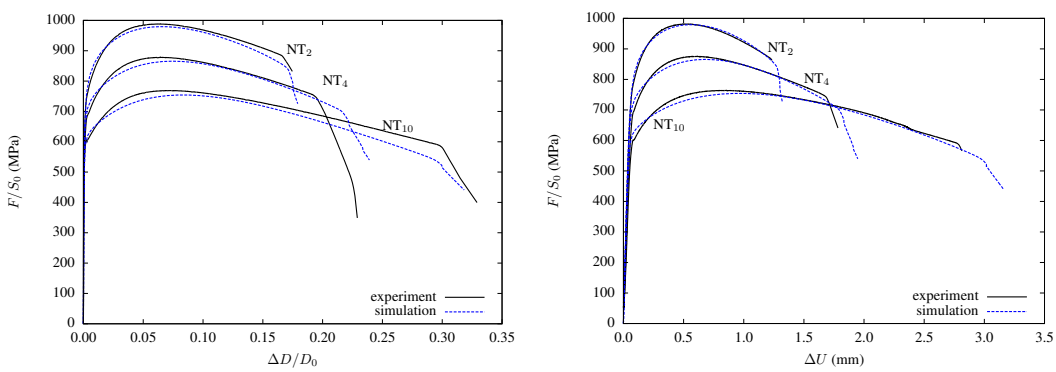

(a) (b)

Figure 15: Comparison of simulated and experimental average stress — relative diameter variation (a) and average stress — displacement (b) curves for NT_2, NT_4 and NT_{10} specimens.

5.4. Model validation on C(T) specimens

The experimental and simulated force—CMOD curves are shown in fig. 16. The simulation corresponds to a test for which the initial crack length was $a_0 = 24.3$ mm. A very good agreement is found. Simulations with von-Mises plasticity (no damage growth) were also carried out. One can see that both simulations start to significantly differ for CMOD ≈ 1 mm. This value can therefore be interpreted as the CMOD for which ductile crack growth starts.

In experiments, the crack length was determined using the unloading compliance technique. In simulations, the crack is defined as the zone where $f = f_R$ (fully broken material). The simulation was then post–processed in order to mimic the ASTM–1820 9-point method in the deformed configuration.

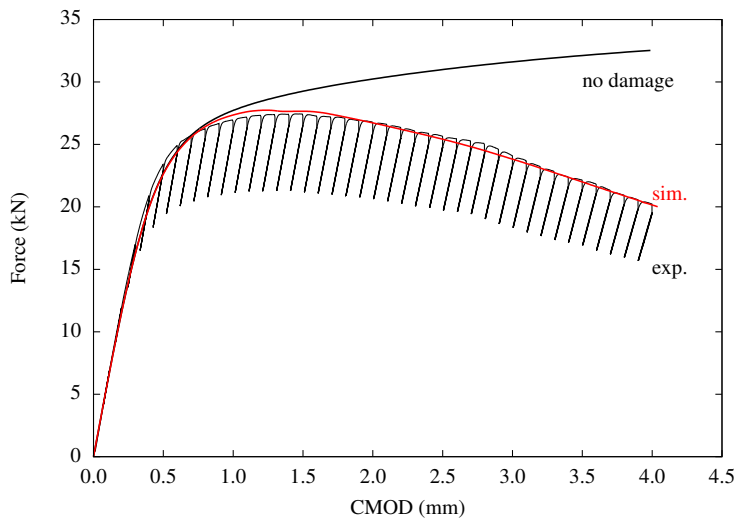

Figure 16: Comparison of the experimental and simulated Force—CMOD curves for compact tension specimens.

Fig. 17–a plots the average crack extension Δa as a function of the CMOD. The experimental crack advance includes initial crack blunting, whereas the simulated crack advance only represents actual ductile tearing. For that reason the experimental crack advance was corrected by removing the CTOD corresponding to $\mathrm{J}_{0.2}$, *i.e.* CTOD $= \frac{1}{2}\mathrm{J}_{0.2}/\sigma_Y$ where σ_Y is the average of the yield stress and the ultimate stress. Both values for crack advance are plotted in fig. 17–a. The agreement with the experimental curve is very good.

The simulated crack front (fig. 17–b) shows a slight curvature with crack growth being larger at the center of the specimen than close to the side–groove. Experimental crack fronts appears however straight (fig. 7). The difference may be linked to the fact that void nucleation is not taken into account in the simulations.

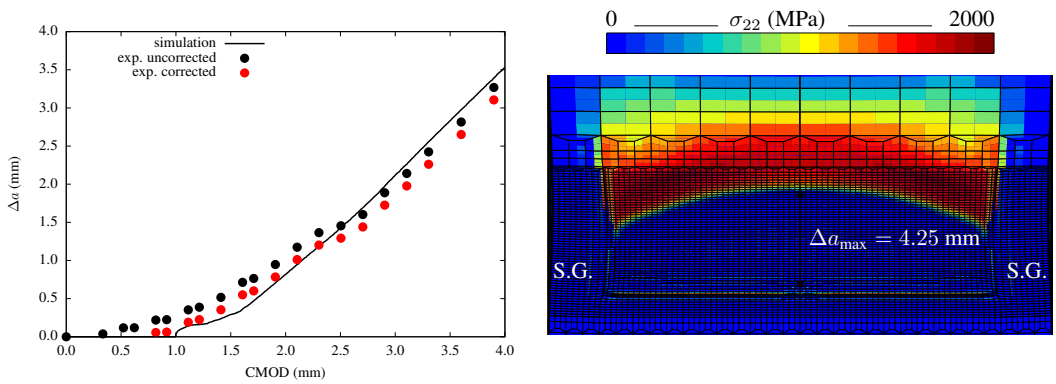

(a) (b)

Figure 17: (a) Comparison of the experimental and simulated Δa—CMOD curves for compact tension specimens. (b) Simulated crack front at CMOD= 4 mm.

6. Simulation of the full scale pipe test

6.1. Mesh and boundary conditions

The mesh for the pipe is shown in fig. 18. Only one quarter of the pipe is modeled to reduce the problem size. In addition since crack bifurcation along two symmetric directions are observed at crack initiation (Fig. 9 and fig. 11), symmetry can be applied. Indeed symmetry is lost after some crack advance. In the refined region ahead of the initial crack tip, the element height (pipe axis direction) is 100 μm as well as the element width (circumferential direction/crack propagation direction). This allows describing the damage localization bands. The element depth (thickness direction) is equal to 830 μm as stress and strain gradients are limited along this direction. This also allows limiting the total number of elements. The mesh is also refined over a height equal to 2.4 mm, so that crack bifurcation from the symmetry plane can be represented. In order to limit the number of unknown the 5–field formulation is only used in a limited volume around the highly refined zone. The resulting mesh for the pipe has $\sim 2,700,000$ degrees of freedom and $\sim 160,000$ elements.

Usual boundary and loading conditions for 4-point bending are used. The central part is modeled using the GTN model while the extension part is assumed to be elastic. During the actual test, loading was achieved through contact between the supports and the pipe. This was neglected in the current simulation where the support was modeled by a linear segment on which the prescribed vertical displacement was applied. To check the validity of this assumption, a pipe without

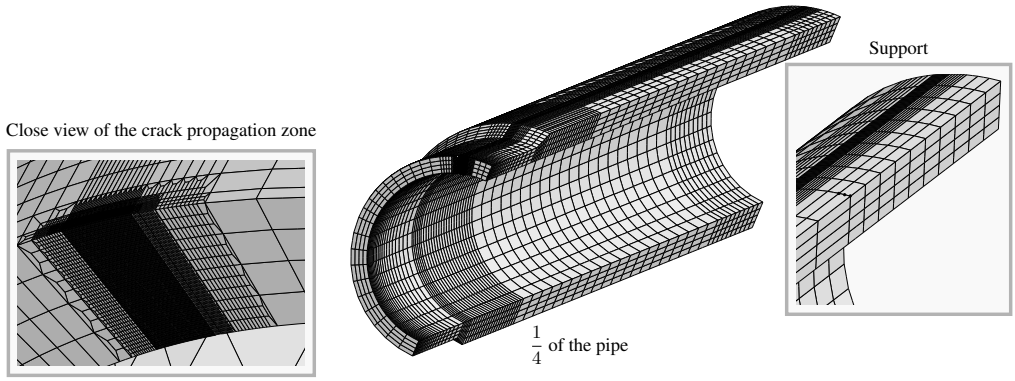

Figure 18: Mesh for the simulation of the full size test.

defect (*i.e.* with much less degrees of freedom) was simulated accounting or not for contact. Both simulations provided very similar results in terms of load and deformation in the tested WB36 segment. However, one should notice that prescribing boundary conditions on a segment is mathematically not correct since it may induce an ill-posed variational problem (one can refer to [**?**] for the detailed explanation). Numerically, this modeling method can induce indentation which strongly affects computational convergence. In the present case, the support is located in the extension parts which are assumed to be elastic. In that case, convergence is thus expected to be unaffected by the simplified modeling of the supports. It was also checked that the yield stress of the E355 material was not exceeded during the simulation except close to the supports.

6.2. Macroscopic response

Fig. 19 plots the experimental and simulated (with GTN and von Mises models) force—CMOD curves for the full size test. It can be observed that the curve obtained with the GTN model starts to slightly deviate from the one obtained with von Mises plasticity for a CMOD of about 2.2 mm. For this value, the simulated crack starts to propagate along the entire crack front. One however notices that both simulated curves (red and blue solid lines) remain very close although a significant crack advance is achieved at the end of the simulation (CMOD$\approx$9.6 mm). This is due to the fact that the simulated crack extension remains small compared to the remaining ligament.

It can also be seen that the simulated result agrees well with the experimental results up to a CMOD≈8 mm. The predicted force is just slightly higher than the experimentally measured one. This difference can be linked to the modeling strategy (the extension arms are assumed to be elastic, contact with the support is not modeled) or to the inhomogeneity of the material. Simulations were not performed for CMOD values greater than 10 mm as the crack was no longer propagating in the predefined fine element zone.

A simulation was also carried out using a local GTN model keeping all material parameters constant. The mesh design is the same but quadratic hexahedra have been replaced by tri-linear hexahedra (8 nodes/8 Gauss points). To avoid pressure fluctuations, the so-called $\overline{\boldsymbol{B}}$ formulation was used [**? ?**]. In that case, the number of degrees of freedom was only $\sim 520,000$. The resulting load—CMOD curve is plotted in fig. 19 (dashed curved). In absence of a non local regularization, damage localization is easier and the crack tends to propagate faster. For that reason the load is smaller than for the simulation with the non local GTN model. This implies that GTN model parameters fitted using a local version of the model cannot be directly used to perform non local simulations. The calculation was stopped for a CMOD equal to 5.5 mm as the crack reached the coarse mesh zone.

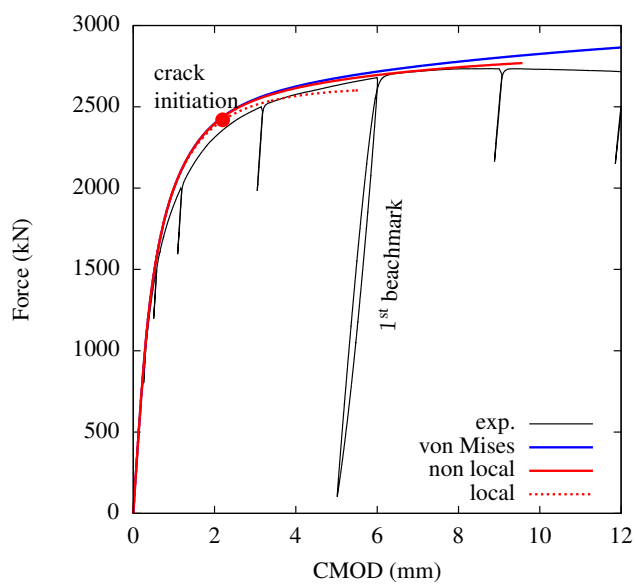

Figure 19: Simulated (with and without damage) and experimental Force—CMOD curves for the full size test.

6.3. Crack extension and crack path

Fig. 20 shows the crack path for a CMOD equal to 9.6 mm. The path is shown for different values of the radius r along the pipe thickness ranging from $r = 159$ mm (internal wall) to $r = 189$ (external wall) in the undeformed configuration. Close to the inner and outer walls, the crack tends to leave the symmetry plane. Due to symmetry, two cracks are actually formed which corresponds to what is experimentally observed for the early stages of crack propagation (see fig. 11). This corresponds to the beginning of crack twisting. At mid-thickness ($r = 175$ mm) the crack remains flat as observed experimentally during the early stages of cracking. The fully flat crack path is observed between $r = 167$ and $r = 183$ mm. This corresponds to the triangular area outlined in blue in fig. 11. In the case of the simulation using a local GTN model (see above) crack deflection is not observed and the crack remains in the elements on the symmetry plane. As already stated, crack deflection is observed close to the inner and outer walls. This corresponds to twist as depicted in fig. 10 and to the beginning of crack propagation in the experiment. Modeling of the entire crack deflection would require to use the required fine mesh ($h \approx l_{\text{nl}}/3$) over a much longer (circumferential direction) and much higher (axial direction) finely refined zone in which the crack can extend. In that case one expects that the crack would propagate parallel to the symmetry plane after significant crack advance. That would correspond to the scenario depicted by dashed lines in fig. 10 (*i.e.* crack advance without tilt). Such a simulation would require about 2 millions elements which corresponds to about 32 millions degrees of freedom. Such a high number of elements, considering the highly nonlinear material behavior, is out of reach for the time being.

No attempt was made to model crack tilting. First, this would require to mesh half a tube (instead of a quarter) which would lead to a hardly tractable simulation. Second, a specially designed mesh would be required to make sure that the crack stays in the finely refined zone (possibly using a trial and error procedure). Finally, the reason for crack tilting remains unclear. It is however thought to be due to a slightly unbalanced loading. To check this hypothesis, it would be required to measure the load on each of the four supporting elements.

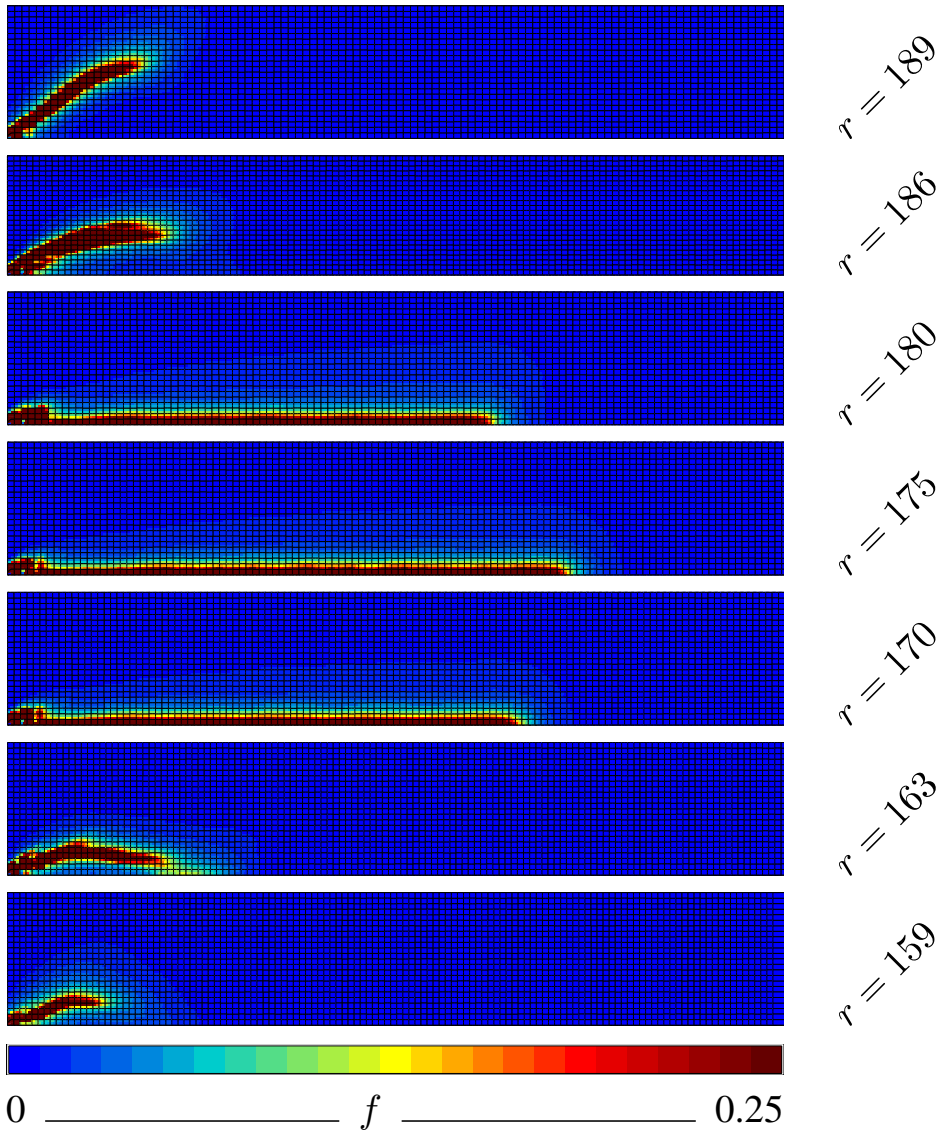

Figure 20: Distribution of porosity f along the circumferential direction for different radii r (mm) when CMOD= 9.6 mm (values at integration points). Plots in the undeformed initial configuration.

6.4. Local stress/strain fields

The crack profile as seen from the axial direction is shown in fig. 21–a for a CMOD equal to 9.6 mm in the deformed state. Elements with more than four Gauss points (GP) where failure occurred have been removed from the plot for clarity. Using this deformed mesh, the cumulated plastic strain at GP is plotted in fig. 21–b. To obtain this plot each cube is divided into 8 smaller cubes which are colored according to the local value to be plotted so as to avoid extrapolation at nodes which can smooth highly irregular solutions otherwise. The nodal counterpart $\overline{\kappa}$ is plotted in fig. 21–c showing a very good match between both quantities. One also observes that plastic strain tends to be higher close to free surfaces (inner and outer diameters). Due to lower triaxiality, more deformation is required to reach failure. Fig. 21–d shows the opening stress at GP which, as expected, is maximum at mid–thickness where crack advance is maximum. Fig. 21–e shows the ratio $\eta^\star = \frac{1}{3}\sigma_{kk}/\sigma_\star$ at GP. This ratio controls the damage growth in the GTN model. Due to damage, $\sigma_\star \geq \sigma_{\text{eq}}$, so that

$$\eta^\star = \frac{1}{3}\frac{\sigma_{kk}}{\sigma_\star} \leq \frac{1}{3}\frac{\sigma_{kk}}{\sigma_{\text{eq}}} = \text{stress triaxiality} \tag{18}$$

Finally, fig. 21–f shows the pressure field (P) at nodes. The three fields exhibit a maximum at mid–thickness. In addition they are regular exhibiting no fluctuations, thus proving the effectiveness of the treatment of volumetric locking.

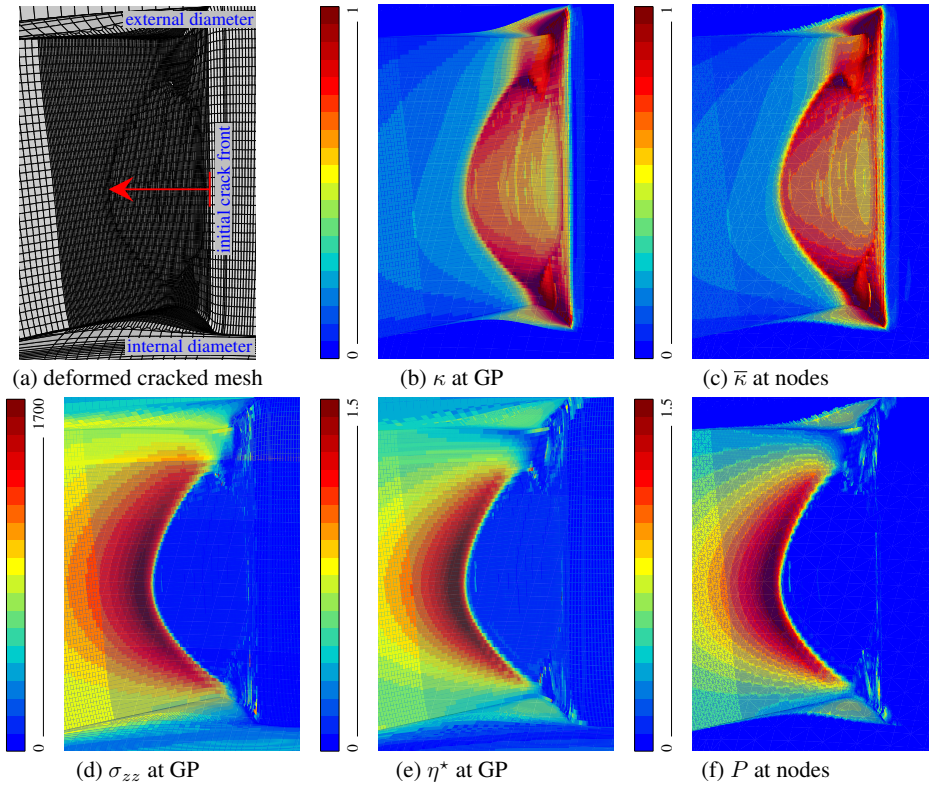

(a) deformed cracked mesh (b) κ at GP (c) $\overline{\kappa}$ at nodes

(d) σ_{zz} at GP (e) $\eta^{\star}$ at GP (f) P at nodes

Figure 21: (a) Crack advance and pipe deformation. The red arrow shows the crack extension at the center of the wall thickness. (b) Contour plots of the hardening variable at Gauss points κ. (c) Contour plots of the hardening variable at nodes $\overline{\kappa}$. (d) Contour plots of the crack opening stress (σ_{zz}). (e) Contour plots of the pseudo–stress triaxiality $\eta^{\star}$. (f) Contour plots of the nodal pressure.

7. Conclusion

In this study a comprehensive mechanical test database on a ferritic steel consisting of tensile tests on notched bars and tests on pre-cracked C(T) specimens is used to fit and validate a non local GTN model. The GTN model is then applied to simulate a large–scale 4–point bending test conducted within the framework of the EU ATLAS+ project.

After fitting, the proposed model is able to reproduce the macroscopic behavior of the test samples. It could be improved so as to obtain a straight crack front during crack propagation in C(T) specimens. This could possibly

be achieved adding void nucleation to the model. However, the macroscopic CMOD—Δa is well reproduced.

The fitted model is then used to simulate the large–scale test. A good agreement is obtained between the simulated and experimental Load—CMOD curves. The simulation requires a large number of element along the crack path with a total number of unknowns equal to 2,700,000. The need to use a fine mesh (100μm) so as to be able to represent the material length scale (300μm) limits the crack extension that can be simulated. However, the model is able to represent crack bifurcation (twist) from the initial crack surface which is experimentally observed. This cannot be reproduced using a local GTN model unless guiding the crack along a predefined path [**?**] using the computational cell methodology [**?** **?**]. Using non local models therefore appears as a promising technique to predict complex crack paths. The simulation technique is also able to eliminate volumetric locking, so that the stress fields ahead of the crack tip can be precisely evaluated.

A possible technique to limit the number of fine elements while allowing for the simulation of large crack extension would be to use remeshing following the work of Mediavilla *et al.* [**?** **?**] (2D) and Javani *et al.* [**?** **?**] (3D). The technique must however be extended so as to be able to deal with degrees of freedom used to control locking. In addition, it will be necessary to coarsen the refined mesh in fully cracked areas as the crack propagates so as to keep the number of unknowns approximatively constant, thus keeping the simulation tractable.

Acknowledgments: This work was carried out within the European project entitled Advanced Structural Integrity Assessment Tools for Safe Long Term Operation (ATLAS+) which has received funding from the Euratom research and training program 2014—2018 under grant agreement No 754589. The project is jointly funded by EU and the individual partners. The authors thank the EU and all the ATLAS+ contributors for their support and contributions.

References

[1] Y. Zhang, E. Lorentz, J. Besson, Ductile damage modelling with locking-free regularised gtn model, Int. J. Numer. Meth. Engng 113 (13) (2018) 1871–1903.

[2] Y. Chen, E. Lorentz, J. Besson, Properties of a nonlocal GTN model within the context of small—scale yielding, Int. J. Plasticity (2020) 102701.

[3] A. Pineau, Development of the local approach to fracture over the past 25 years: theory and applications, Int. J. Frac. 138 (1-4) (2006) 139–166.

[4] J. Besson, Continuum models of ductile fracture: a review, Int. J. Damage Mech. 19 (2010) 3–52.

[5] A. Pineau, A. A. Benzerga, T. Pardoen, Failure of metals I: Brittle and ductile fracture, Acta Mater. 107 (2016) 424–483.

[6] A. Benzerga, J.-B. Leblond, A. Needleman, V. Tvergaard, Ductile failure modeling, Int. J. Frac. 201 (1) (2016) 29–80.

[7] J. Rice, The mechanics of earthquake rupture. Proceedings of the international school of physics "Enrico Fermi", North-Holland, 1980, pp. 555–649.

[8] J. Besson, D. Steglich, W. Brocks, Modeling of crack growth in round bars and plane strain specimens, Int. J. Solids Structures 38 (46–47) (2001) 8259–8284.

[9] G. Rousselier, Ductile fracture models and their potential in local approach of fracture, Nucl. Eng. Des. 105 (1987) 97–111.

[10] L. Xia, C. F. Shih, Ductile crack growth — I. A numerical study using computational cells with microstructurally-based length scales, J. Mech. Phys. Solids 43 (1995) 233–259.

[11] R. Peerlings, R. De Borst, W. Brekelmans, J. De Vree, I. Spee, Some observations on localisation in non–local and gradient damage models, Eur. J. Mech./A 15A (6).

[12] M. Geers, R. de Borst, W. Brekelmans, R. Peerlings, Strain-based transient-gradient damage model for failure analyses, Comp. Meth. Appl. Mech. Engng 160 (1998) 133–153.

[13] G. Pijaudier-Cabot, Z. P. Bazant, Nonlocal damage theory, J. Engrg. Mech. 113 (1987) 1512–1533.

[14] Z. Bazant, G. Pijaudier-Cabot, Non local continuum damage. localization, instability and convergence, J. Applied Mech. 55 (1988) 287–294.

[15] K. Enakoutsa, J. Leblond, G. Perrin, Numerical implementation and assessment of a phenomenological nonlocal model of ductile rupture, Comp. Meth. Appl. Mech. Engng 196 (13-16) (2007) 1946–1957.

[16] J. Mediavilla, R. Peerlings, M. Geers, A nonlocal triaxiality-dependent ductile damage model for finite strain plasticity, Comp. Meth. Appl. Mech. Engng 195 (2006) 4617–4634.

[17] T. Linse, G. Hütter, M. Kuna, Simulation of crack propagation using a gradient-enriched ductile damage model based on dilatational strain, Eng. Fract. Mech. 95 (2012) 13–28.

[18] G. Hütter, T. Linse, U. Mühlich, M. Kuna, Simulation of ductile crack initiation and propagation by means of a non-local Gurson-model, Int. J. Solids Structures 50 (2013) 662–671.

[19] H. Javani, R. Peerlings, M. Geers, Three-dimensional finite element modeling of ductile crack initiation and propagation, Adv. Model. and Simul. in Eng. Sci. (2016) 3–19.

[20] A. Seupel, G. Hütter, M. Kuna, On the identification and uniqueness of constitutive parameters for a non-local GTN-model, Eng. Fract. Mech. 229 (2020) 106817.

[21] S. Forest, Micromorphic approach for gradient elasticity, viscoplasticity, and damage, J. Eng. Mech. 135 (2009) 117–131.

[22] T. Brepols, S. Wulfinghoff, S. Reese, Gradient-extended two-surface damage-plasticity: Micromorphic formulation and numerical aspects, Int. J. Plasticity 97 (2017) 64–106.

[23] E. Diamantopoulou, W. Liu, C. Labergere, H. Badreddine, K. Saanouni, P. Hu, Micromorphic constitutive equations with damage applied to metal forming, Int. J. Damage Mech. 26 (2) (2017) 314–339.

[24] G. Huetter, A micromechanical gradient extension of gurson's model of ductile damage within the theory of microdilatational media, Int. J. Solids Structures 110-111 (2017) 15–23.

[25] E. Lorentz, S. Andrieux, A variational formulation for nonlocal damage models, Int. J. Plasticity 15 (2) (1999) 119–138.

[26] J.-M. Scherer, V. Phalke, J. Besson, S. Forest, J. Hure, B. Tanguy, Lagrange multiplier based vs micromorphic gradient-enhanced rate-(in)dependent crystal plasticity modelling and simulation, Comp. Meth. Appl. Mech. Engng 372 (2020) 113426.

[27] V. Tvergaard, A. Needleman, Analysis of the cup–cone fracture in a round tensile bar, Acta Metall. 32 (1984) 157–169.

[28] R. Taylor, A mixed-enhanced formulation for tetrahedral finite elements, Int. J. Numer. Meth. Engng 47 (2000) 205–227.

[29] T. Hughes, The finite element method: Linear static and dynamic finite element analysis, Prentice–Hall Inc., 1987.

[30] A. S. Gullerud, X. Gao, R. H. Dodds Jr, R. Haj-Ali, Simulation of ductile crack growth using computational cells: numerical aspects, Eng. Fract. Mech. 66 (2000) 65–92.

[31] J. Besson, C. McCowan, E. Drexler, Modeling flat to slant fracture transition using the computational cell methodology, Eng. Fract. Mech. 104 (2013) 80–95.

[32] D. Al Akhrass, J. Bruchon, S. Drapier, S. Fayolle, Integrating a logarithmic-strain based hyperelastic formulation into a three-field mixed finite element formulation to deal with incompressibility in finite-strain elastoplasticity, Finite Elements in Analysis and Design 86 (2014) 61–70.

[33] D. Novokshanov, B. Döbereiner, M. Sharaf, S. Münstermann, J. Lian, A new model for upper shelf impact toughness assessment with a computationally efficient parameter identification algorithm, Eng. Fract. Mech. 148 (2015) 281–303.

[34] M. K. Samal, M. Seidenfuss, E. Roos, A new mesh-independent Rousselier's damage model: Finite element implementation and experimental verification, Int. J. Mech. Sci. 51 (8) (2009) 619–630.

[35] G. Hütter, T. Linse, U. Mëlich, M. Kuna, Simulation of ductile crack initiation and propagation by means of a non-local gurson-model, Int. J. Solids Structures 50 (5) (2013) 662–671.

[36] J. Leclerc, V. Nguyen, T. Pardoen, L. Noels, A micromechanics-based non-local damage to crack transition framework for porous elastoplastic solids, Int. J. Plasticity 127.

[37] A. Remmal, V. Paraskevaidis, S. Marie, A. Blouin, S. Chapuliot, Prediction of ductile crack growth in a narrow gap Inconel dissimilar weld, Int. J. of Pressure Vessels and Piping 173 (2019) 94–100.

[38] J. R. Rice, D. M. Tracey, On the ductile enlargement of voids in triaxial stress fields, J. Mech. Phys. Solids 17 (1969) 201–217.

[39] C. Oh, Y. Kim, J. Baek, W. Kim, Development of stress-modified fracture strain for ductile failure of API X65 steel, Int. J. Frac. 143 (2007) 119–133.

[40] B. Medjo, M. Rakin, N. Gubeljak, Y. Matvienko, M. Arsić, Ž. Šarkoćević, A. Sedmak, Failure resistance of drilling rig casing pipes with an axial crack, Eng. Fail. Anal. 58 (2) (2015) 429–440.

[41] T. Nicak, H. Schendzielorz, E. Keim, G. Meier, STYLE: Study on transferability of fracture material properties from small scale specimens to a real component, in: Duncan, A.J. (Ed.), Proceedings of the asme pressure vessels and piping conference, PVP 2011, Vol. 6, A and B, ASME, Pressure Vessels & Pip Div, 2012, pp. 313–322.

[42] N. Nourpanah, F. Taheri, Ductile crack growth and constraint in pipelines subject to combined loadings, Eng. Fract. Mech. 78 (9) (2011) 2010–2028.

[43] K. Jayadevan, E. Berg, C. Thaulow, E. Østby, B. Skallerud, Numerical investigation of ductile tearing in surface cracked pipes using line-springs, Int. J. Solids Structures 43 (7-8) (2006) 2378–2397.

[44] H. Tang, D. Fairchild, M. Panico, J. Crapps, W. Cheng, Strain capacity prediction of strain-based pipelines, in: Proceedings of the 10th international pipeline conference — 2014, Vol 4, ASME, 2014.

[45] C. Soret, Y. Madi, V. Gaffard, J. Besson, Local approach to fracture applied to the analysis of a full size test on a pipe containing a girth weld defect, Eng. Fail. Anal. 82 (2017) 404–419.

[46] C. Defaisse, M. Mazière, L. Marcin, J. Besson, Ductile fracture of an ultra-high strength steel under low to moderate stress triaxiality, Eng. Fract. Mech. 194 (2018) 301–318.

[47] K. Decamp, L. Bauvineau, J. Besson, A. Pineau, Size and geometry effects on ductile rupture of notched bars in a C–Mn steel: Experiments and modelling, Int. J. Frac. 88 (1) (1997) 1–18.

[48] J. Hancock, A. Mackenzie, Mechanisms of ductile failure in high-strength steels subjected to multi- axial stress states, J. Mech. Phys. Solids 24 (1976) 147–160.

[49] B. Marini, F. Mudry, A. Pineau, Ductile rupture of A508 steel under nonradual loading, Eng. Fract. Mech. 22 (3) (1985) 375–386.

[50] A. Mackenzie, J. Hancock, D. Brown, On the influence of state of stress on ductile failure initiation in high strength steels, Eng. Fract. Mech. 9 (1977) 167–188.

[51] F. Bron, J. Besson, A. Pineau, Ductile rupture in thin sheets of two grades of 2024 aluminum alloy, Mater. Sci. Engng A 380 (2004) 356–364.

[52] F. Bron, J. Besson, Simulation of the ductile tearing for two grades of 2024 aluminum alloy thin sheets, Eng. Fract. Mech. 73 (2006) 1531–1552.

[53] S. El-Naaman, K. Nielsen, Observations on Mode I ductile tearing in sheet metals, Eur. J. Mech./A 42 (2013) 54–62.

[54] C. Miehe, N. Apel, M. Lambrecht, Anisotropic additive plasticity in the logarithmic strain space: modular kinematic formulation and implementation based on incremental minimization principles for standard materials, Comp. Meth. Appl. Mech. Engng 191 (2002) 5383–5425.

[55] C. Miehe, M. Lambrecht, Algorithms for computation of stresses and elasticity moduli in terms of Seths—Hill's family of generalized strain tensors, Commun. Numer. Meth. Engng 17 (2001) 337–353.

[56] P. Germain, Q. Nguyen, P. Suquet, Continuum thermodynamics, J. Applied Mech. 5 (1983) 1010–1020.

[57] E. Lorentz, J. Besson, V. Cano, Numerical simulation of ductile fracture with the rousselier constitutive law, Comp. Meth. Appl. Mech. Engng 197 (21-24) (2008) 1965–1982.

[58] M. Fortin, R. Glowinski, Augmented Lagrangian Methods: Applications to the Numerical Solution of Boundary-Value Problems, Elsevier, 1893.

[59] H.-C. Hu, On some variational principles in the theory of elasticity and plasticity, Sci. Sin. 4 (1955) 33–54.

[60] C. Chu, A. Needleman, Void nucleation effects in biaxially stretched sheets, J. Engng Mater. Technol. 102 (1980) 249–256.

[61] B. Tanguy, T. Luu, G. Perrin, A. Pineau, J. Besson, Plastic and damage behavior of a high strength X100 pipeline steel: experiments and modelling, Int. J. of Pressure Vessels and Piping 85 (5) (2008) 322–335.

[62] A. Bertram, Elasticity and Plasticity of Large Deformations, Springer, 2012.

[63] L. Cortese, T. Coppola, F. Campanelli, G. Broggiato, A J_2–J_3 approach in plastic and damage description of ductile materials, Int. J. Damage Mech. 25 (2) (2016) 228–250.

[64] J. Papasidero, V. Doquet, D. Mohr, Ductile fracture of aluminum 2024-T351 under proportional and non-proportional multi-axial loading: Bao–Wierzbicki results revisited, Int. J. Solids Structures 69–70 (2015) 459–474.

[65] Y. Li, T. Wierzbicki, Prediction of plane strain fracture of AHSS sheets with post-initiation softening, Int. J. Solids Structures 47 (17) (2010) 2316–2327.

[66] K. Nahshon, J. Hutchinson, Modification of the Gurson model for shear failure, Eur. J. Mech./A 27A (2008) 1–17.

[67] K. L. Nielsen, V. Tvergaard, Effect of a shear modified Gurson model on damage development in a FSW tensile specimen, Int. J. Solids Structures 46 (3-4) (2009) 587–601.

[68] V. Davaze, N. Vallino, B. Langrand, J. Besson, S. Feld-Payet, A non-local damage approach compatible with dynamic explicit simulations and parallel computing, Int. J. Solids Structures 228 (2021) 110999.

[69] V.-D. Nguyen, T. Pardoen, L. Noels, A nonlocal approach of ductile failure incorporating void growth, internal necking, and shear dominated coalescence mechanisms, J. Mech. Phys. Solids 137 (2020) 103891.

[70] J. Besson, R. Foerch, Large scale object–oriented finite element code design, Comp. Meth. Appl. Mech. Engng 142 (1997) 165–187.

[71] R. Foerch, J. Besson, G. Cailletaud, P. Pilvin, Polymorphic constitutive equations in finite element codes, Comp. Meth. Appl. Mech. Engng 141 (1997) 355–372.

[72] A. G. Franklin, Comparison between a quantitative microscope and chemical methods for assessment of non–metallic inclusions, J. Iron Steel Inst. Feb. (1969) 181–186.

[73] J. Koplik, A. Needleman, Void growth and coalescence in porous plastic solids, Int. J. Solids Structures 24 (8) (1988) 835–853.

[74] Y. Shinohara, Y. Madi, J. Besson, Anisotropic ductile failure of a high-strength line pipe steel, Int. J. Frac. 197 (2016) 127–145.

[75] E. Lorentz, Ill-posed boundary conditions encountered in 3d and plate finite element simulations, Finite Elem. Anal. Des. 41 (11-12) (2005) 1105–1117.

[76] T. Hughes, Generalization of selective integration procedures to anisotropic and non linear media, Int. J. Numer. Meth. Engng 15 (1980) 1413–1418.

[77] L. Xia, C. F. Shih, Ductile crack growth — II. Void nucleation and geometry effects on macroscopic fracture behaviour, J. Mech. Phys. Solids 43 (1995) 1953–1981.

[78] J. Mediavilla, R. Peerlings, M. Geers, Discrete crack modelling of ductile fracture driven by non-local softening plasticity, Int. J. Numer. Meth. Engng 66 (4) (2006) 661–688.

[79] J. Mediavilla, R. Peerlings, M. Geers, A robust and consistent remeshing-transfer operator for ductile fracture simulations, Computers & Structures 84 (8-9) (2006) 604–623.

[80] A. Javani, R. Peerlings, M. Geers, Consistent remeshing and transfer for a three dimensional enriched mixed formulation of plasticity and non-local damage, Comput. Mech. 53 (2014) 625–639.

List of Figures

1 Microstructure of the WB36 material. 6
2 Geometries of the smooth tensile specimen ST6, Notch tensile specimens NT_2, NT_4 and NT_{10} (unit: mm). 8
3 Full size test (FP1 pipe). 9
4 EDF R&D 4–point bending frame for testing mock-ups (length units in mm): (a) Overall view of the setup. (b) 4–point bending test showing the pipe and the four indentical rollers. (c) Detailed view of the diabolo–shaped rollers. 9
5 Stress—strain curves for the WB36 pipe material. 13 tests are shown. 10
6 NT_χ tests. (a) Average stress — axial displacement curves. (b) Average stress — relative diameter reduction curves. Solid lines: video system. Dashed lines: extensometer. 12
7 C(T)20 tests. (a) Force—CMOD curves. The red curve corresponds to the specimen shown in (b). (b) Macroscopic view of ductile crack extension (dark area). 13
8 (a) View of the pipe during the test. Pipe deflection is clearly visible. (b) Force—CMOD curves. 14
9 Outer view of the cracked pipe after the test was stopped showing both mains cracks and secondary cracks. 15
10 (a) 3D scan of the initial defect and crack propagation. (b) Schematic view of the crack path. The blue lines indicate the crack path on the external (thick lines) and internal (thin lines) diameters of the pipe. The thin green dashed lines represent the crack path in absence of tilt. Red dots indicate the position of the seven potential drop measurements. 16
11 View of crack bifurcation at both ends of the initial crack after the paper was 17
12 Examples of non local locking–free finite elements with reduced integration: quadrilateral element and triangular element 20
13 Meshes for (a) NT_2, NT_4, NT_{10} and (b) C(T)20 specimens. 23
14 Simulation of the NT_2 specimen with various mesh sizes. Contour plots show values of the opening stress (MPa) and damage during crack propagation from the center of the specimen. 25

15 Comparison of simulated and experimental average stress — relative diameter variation (a) and average stress — displacement (b) curves for NT_2, NT_4 and NT_{10} specimens. 26
16 Comparison of the experimental and simulated Force—CMOD curves for compact tension specimens. 27
17 (a) Comparison of the experimental and simulated Δa—CMOD curves for compact tension specimens. (b) Simulated crack front at CMOD$= 4$ mm. 28
18 Mesh for the simulation of the full size test. 29
19 Simulated (with and without damage) and experimental Force—CMOD curves for the full size test. 30
20 Distribution of porosity f along the circumferential direction for different radii r (mm) when CMOD$= 9.6$ mm (values at integration points). Plots in the undeformed initial configuration. . 32
21 (a) Crack advance and pipe deformation. The red arrow shows the crack extension at the center of the wall thickness. (b) Contour plots of the hardening variable at Gauss points κ. (c) Contour plots of the hardening variable at nodes $\overline{\kappa}$. (d) Contour plots of the crack opening stress (σ_{zz}). (e) Contour plots of the pseudo–stress triaxiality $\eta^\star$. (f) Contour plots of the nodal pressure. 34

List of Tables

1 Chemical composition (wt. %) of the 15NiCuMoNb5 ferritic steel (WB36). 6
2 Chemical composition (wt. %) of the extension pipe (E355). . . . 6
3 Tensile properties of the bending arms material (E355) at room temperature. E: Young's modulus, $R_{p0.2}$: 0.2% proof strength, R_m: ultimate stress, e_R: elongation at fracture, Z: reduction of area. 11
4 Material parameters. 25